# V-shape plasma generated by excimer laser ablation of graphite in argon: Spectroscopic investigations

C. Ursu, P. Nica, B.G. Rusu, C. Focsa

# V-shape plasma generated by excimer laser ablation of graphite in argon: Spectroscopic investigations

**C. Ursu[1], P. Nica[2,*], B. G. Rusu[1], and C. Focsa[3]**

[1] *"Petru Poni" Institute of Macromolecular Chemistry, 41 A Gr. Ghica Voda Alley, Iasi 700487, Romania*
[2] *Department of Physics, "Gheorghe Asachi" Technical University, Iasi, 700050, Romania*
[3] *Univ. Lille, CNRS, UMR 8523, PhLAM – Physique des Lasers, Atomes et Molécules, CERLA – Centre d'Etudes et de Recherches Lasers et Applications, F-59000 Lille, France*
**Corresponding author*: pnica@tuiasi.ro

**Abstract:**

Continuing previous works on the dynamics of carbon plasmas generated by excimer laser ablation in vacuum, we report here a new study using Ar as background gas. The increased collision rate allows extended (both spatially and temporally) investigations of the low-emitting axial region of the unusual V-shape transient plasma evidenced in our previous works. The systematic study performed here by fast-gate intensified CCD photography and space- and time-resolved optical emission spectroscopy led to an extensive database, especially on the evolution of C, Ar and C-dimer (monitored through the Swan bands). The enhancement of the dimer formation (which has an important role in carbon plasma chemistry) in the lateral structures is confirmed and even amplified by the use of background gas. Furthermore, temperature and electron density values have been estimated from the spectroscopic data, providing additional proofs for the validity of the plasma dynamics scenario built for this unusual plume shape.

**Keywords**: Excimer laser ablation, Carbon plasma, Optical emission spectroscopy, Carbon dimer, Plasma dynamics

## 1. Introduction

Sustained efforts devoted to a better fundamental understanding of the complex phenomena related to laser ablation and laser-produced plasmas (including, *e.g.*, investigation of laser parameters influence on plasma dynamics and laser-target interaction [1-3]) have led over the last decades to the development of a wide variety of applications in very diverse fields, such as laser surgery in medicine, welding and cutting in automotive industry, precision micro-fabrication, new laser-based concepts for space propulsion, etc. Detailed investigations on the fast transient laser-produced plasma plume have contributed to the spreading out of powerful analytic tools such as Laser-Induced Breakdown Spectroscopy (LIBS) [4,5] or to the optimization of the Pulsed Laser Deposition (PLD) technique for the synthesis of nanoscale thin films with numerous applications [6–9].

In this latter field, studying carbon plasma produced by graphite target ablation with lasers of various wavelengths and temporal regimes is of great interest for the synthesis of materials with high applicative potential, such as diamond, fullerenes, nanotubes or graphene [10–12]. Beside the ablation laser characteristics, other process parameters can have a significant influence on the synthesized material quality. For instance, the background gas pressure was shown to highly impact the structural properties of the PLD diamond like carbon (DLC) films: a high content of $sp^3$ bonds (characterizing DLC), was obtained at pressures below 200mTorr, while above this value the amount of $sp^2$ bonds (specific of amorphous carbon) is more significant [13,14]. Ablated species velocity distribution and ionization degree are other key factors known to directly influence the deposited film properties [15,16]. In this context, the optical emission spectroscopy (OES) is a most convenient, non-invasive method used to gather information on the

* Author for correspondence: email: pnica@tuiasi.ro

space-time evolution of plasma individual species (*i.e.* composition of plasma, velocity distribution of generated species, etc.) [17,18]. For the specific case of carbon plasmas, a major-interest player is the carbon dimer ($C_2$), especially for its role in the formation of large molecules, which are assumed to be created by $C_2$-chaining [19,20]. The well-known $d^3\Pi_g \rightarrow a^3\Pi_g$ Swan system [21] offers a suitable opportunity for monitoring the $C_2$ formation and evolution by OES in the visible spectral range.

In previous works [22–24] we revealed the occurrence of an unusual V-shape transient carbon plasma produced by excimer laser ablation of graphite in vacuum. Extensive experimental evidence on the enhancement of carbon dimer formation in this plasma has been brought by combining fast-gate ICCD imaging, OES, Faraday cup ion measurements and ablation crater depth profiling [24]. A theoretical model was also developed [25] in a fractal-based approach [26]. In these previous works, we connected the unusual shape of the plasma emission with the irradiance distribution in the excimer laser beam. However, very recent (unpublished) studies performed with a Nd:YAG laser [27] seem to evidence a universal character of the enhanced emission at the periphery of the plasma. Considering $C_2$ is the prominent emitter in the carbon plasma, the observation of such an unusual shape could be due to rapid cooling at the periphery of the plasma with ambient gas interaction and subsequent dimer formation. We note that a V-shaped structure was also observed during Nd:YAG ablation in the presence of a magnetic field [28], which led the authors to explain its occurrence through magnetic confinement effects. Similar structures can be seen in [29], although no explanation was provided for their origin.

In the present paper, we continue these investigations by a systematic optical and spectroscopic study on the V-shape carbon plasma generated in Ar background gas. The enhancement of the collisional processes brought by the Ar gas gives access to a better characterization (through ICCD fast imaging and time- and space-resolved optical emission spectroscopy) of the low-emitting axial region of the V-shape plasma. Spectral features of atomic C, Ar and molecular $C_2$ (Swan bands) were monitored on extended spatial (axial and radial) ranges and for long delays after the ablation pulse. Furthermore, plasma temperature and electron density calculations have been performed in order to better describe the various structures dynamics and to highlight the role of the ambient gas in the overall evolution scenario.

## 2. Experimental details

The V-shape carbon plasma is generated through KrF excimer laser ablation of a pyrolytic graphite target in 5 Pa argon gas environment. A detailed description of the experimental setup is given in [24], we only recall the main elements here. The laser beam with a typical energy profile (top-hat on the long axis, and approximately Gaussian on the short axis) was focused on the target at 45° incidence through a spherical lens of 0.5 m focal distance, without additional optics for beam shaping or homogenizing. The working pressure and the laser fluence (2.1 J/cm$^2$) were kept constant during the measurements. The distance between the focusing lens and the target was maintained at $LP$=46 cm, which previously led to the V-shape plasma formation for ablation in vacuum [24]. 2D snapshots of expanding plasma were recorded with an Andor iStar ICCD camera at 50 ns gate width. Features corresponding to different time delays and space regions are investigated by OES using the same gate width and 1 mm space-resolution. The spectral measurements were made by using a 33 cm focal length monochromator (Shamrock SR-303I-A) fitted with a 600 lines/mm grating, with an instrumental broadening of 0.25 nm. The spectrally resolved transient optical signal was recorded for five spots along the target normal ($z$=2.5 mm, $z$=5 mm, $z$=7.5 mm, $z$=10 mm, and $z$=12.5 mm) and four points along the radial direction ($x$=5 mm, $x$=7.5 mm, $x$=10 mm, and $x$=12.5 mm), as indicated below by the open circles in Fig. 1. With respect to the *Oxyz* coordinate system displayed in the top left panel of Fig. 1, the target is located in the *xOy*-plane, the laser beam is incident in the *yOz*-plane at 45° with respect to the *z*-axis, and the long and short axes of the laser spot correspond to *Ox* and *Oy* axes, respectively. The plasma emission is recorded from the *xOz*-plane.

## 3. Results and discussion

### *3.1. Plasma ICCD imaging and global expansion velocities*

The ICCD images (Fig. 1) recorded at different delays reveal the V-shape plasma structure that can be observed after the initial stages of expansion, similarly as in vacuum. Along the normal direction to the target surface, there are initially fast ejected particles which are decelerated by the ambient gas [30,31] (see the arc-shape emitting region for example at 0.6 μs), leaving behind two radiating lateral arms. Such two types of ejected particles (structures) are well-known, being formed through distinct mechanisms, *i.e.* acceleration in the self-generated electric field given by charge separation at early stages, and then ejection through thermal processes, respectively [32-34]. At later times, after about 2 μs, these arms transform in two plasma balls, flying almost parallel with the target normal, until they finally merge in a single structure. We note that each image from Fig. 1 was normalized to its maximum intensity, for a better observation of the plasma evolution, while the total plasma emission decreased with time.

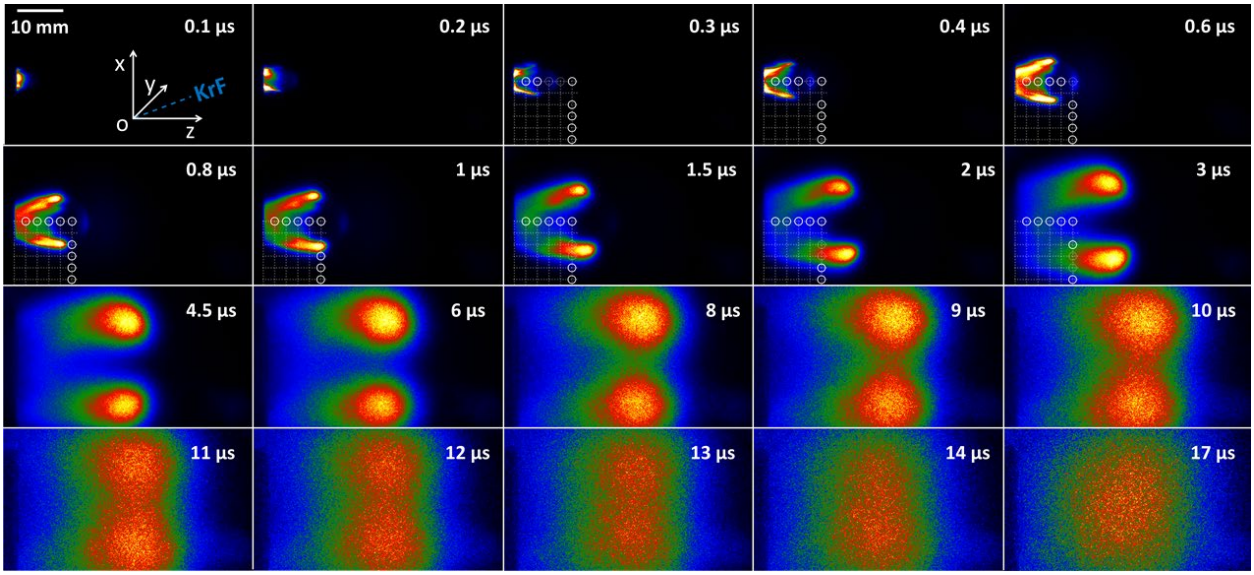


**Fig. 1.** Fast-gate (50 ns) ICCD images of V-shape carbon plasma expanding in argon gas (circles indicate the regions used for OES measurements).

By cross-sectioning ICCD images, one obtains the maximum emissivity coordinates of the fast central structure and of the slow lateral ones (red and black spots, respectively, in Fig. 2a). Then, plotting them *vs*. delay – Fig. 2b, we obtain initial linear dependences for delays lower than 0.7 μs and 2 μs, respectively. The corresponding velocities are $v_{fast}\left(v_{fast}^{x}, v_{fast}^{z}\right) = (0, 1.5)\cdot 10^{4}\mathrm{m/s}$, and $v_{slow}(v_{slow}^{x}, v_{slow}^{z}) = (2.1, 6.2)\cdot 10^{3}\mathrm{m/s}$. After the initial stages both structures are slowed down and tend to similar $z$-positions in time (see dotted curve in Fig. 2b). The time-dependence of the maximum emissivity positions obeys the well-known drag model [35,36], as previously shown in [24].

We note that for higher irradiation regimes [37] (for example by using tighter focusing or shorter pulse durations), or for a different target material, a better velocity separation is obtained between the faster particles ejected through electrostatic mechanisms and the slower ones resulted from the subsequent thermal processes.

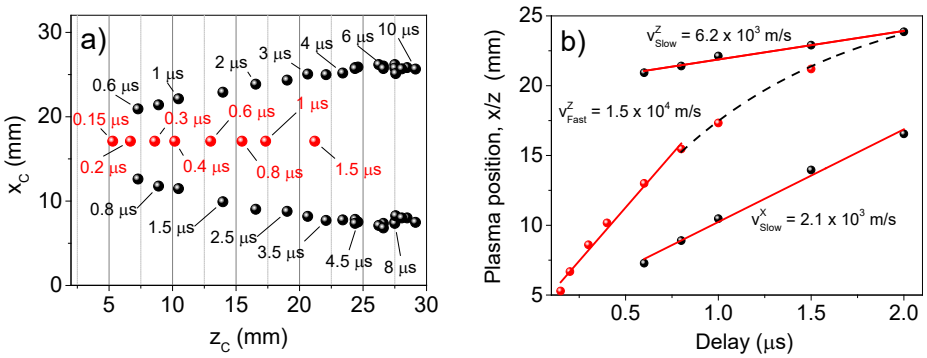


**Fig. 2.** a) Space position of maximum emission intensity at various time delays for the fast central plasma (red spot) and the slow lateral structures (black spot) and b) resulting expansion velocities.

*3.2. Space-time evolution of plasma species*

To get more insight on the plasma components evolution, the atomic and ionic species were tracked by using time-resolved OES of ≈1 mm$^2$ emitting regions of plasma, along the *Ox* and *Oz* axes. The recording gate time of 50 ns and accumulation for 100 laser pulses ensured a good signal-to-noise ratio for all plasma species in the considered experimental conditions and allowed to obtain a low level of continuum (broadband) emission. In Fig. 3, typical spectra for the two investigated spectral ranges are presented for $z$=12.5 mm from the target and two $x$-distances from the plasma symmetry plane ($yOz$). The displayed spectra are « raw data » (i.e. "as recorded"), however, sensitivity calibration was applied when using individual lines intensities in temperature calculations (see below). They reveal the presence of $C_2$ molecules through the Swan bands corresponding to the transitions between the vibrational levels described by $\Delta v = -1,0,1,2$, with $v$ the vibrational quantum number, in the spectral range between 430 nm and 570 nm (Fig. 3a). Several emission lines are identified based on [38] as corresponding to atomic C, Ar, and $C^+$ (less intense) species, in the spectral range between 700 nm and 840 nm (Fig. 3b), where vibrational-rotational transitions are absent. Among them, $\lambda$=833.5 nm (C), $\lambda$=811.5 nm (Ar) and $\lambda$=416.5 nm ($C_2$) are further monitored, being considered as relevant for corresponding species evolution. An interesting feature revealed by Fig. 3a (to be used in the following) is the clear reduction of atomic C emission with respect to the $C_2$ bands intensity, when going off-axis (red curve).

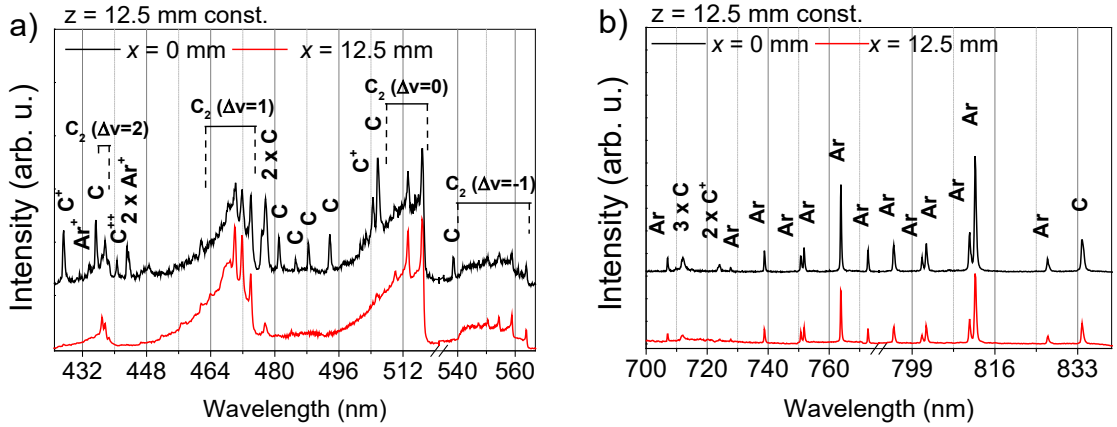


**Fig. 3.** Typical plasma emission spectra recorded at $z$=12.5 mm away from the target, on the plasma symmetry axis ($x$=0, black curves), and at $x$=12.5 mm in radial direction (red curves) corresponding to a) $C_2$ Swan system and b) atomic Ar spectral regions, respectively.

In Fig. 4a,b, the time-resolved spectra at $z$=12.5 mm from the target, recorded for various delays, show the presence of a maximum emissivity of each plasma component, at distinct times (see thicker

curves). When extracting the time-evolution of relevant lines intensities at various distances, this conclusion becomes clearer: atomic C is mostly present near the target, at early times, while the dimer persists for longer times and distances. Most of the Ar emission occurs, as expected, far away from the target. The emission of Ar lines can be seen at high distance even at early times, and most probably this is due to the photo-excitation processes induced by high-energy photons emitted by the plume at the initial stages of its expansion. We note however that simple atomic collisions are not to be excluded. Indeed, the ejected atoms (and ions) exhibit a velocity distribution which can contain a minority of high-speed species in the high-energy tail. For instance, species with $2.5\times10^5$ m/s (not so uncommon, especially for ions) can travel the 12.5 mm distance in 50 ns. On the other hand, the maximum emission observed can be related with the maximum of the velocity distribution of ejecta. Indeed, the maximum intensity of the Ar 811.5 nm line is recorded at $z$=12.5 mm after about 0.6 μs (Figure 4c), which is very close to the ≈700 ns needed by most of the plasma species to reach 12.5 mm, as it can be observed from velocity measurement based on ICCD images. In our opinion, this maximum is given by excitation processes brought by collisions with the plume particles.

In [24] we deduced a linear dependence for position *vs.* time for maximum intensity, but this is valid only for vacuum expansion, and not in the ambient gas as in the present experiments. Also, we can infer a significant difference when comparing with the results from [24], where "the most significant emission of $C_2$ is near the target surface, while CI and CII are observed up to tens of millimeters away.", that allowed us to conclude: "for the fast-central part of the plasma most of the $C_2$ molecules are the result of three-body recombination processes". The present observations imply distinct mechanisms for the production and the excitation of plasma species: neutral carbon and its singly-charged ion are directly ejected at initial stages, the dimers are formed in the slow plasma tail, while Ar excitation is the result of collisions with the fast plasma structure.

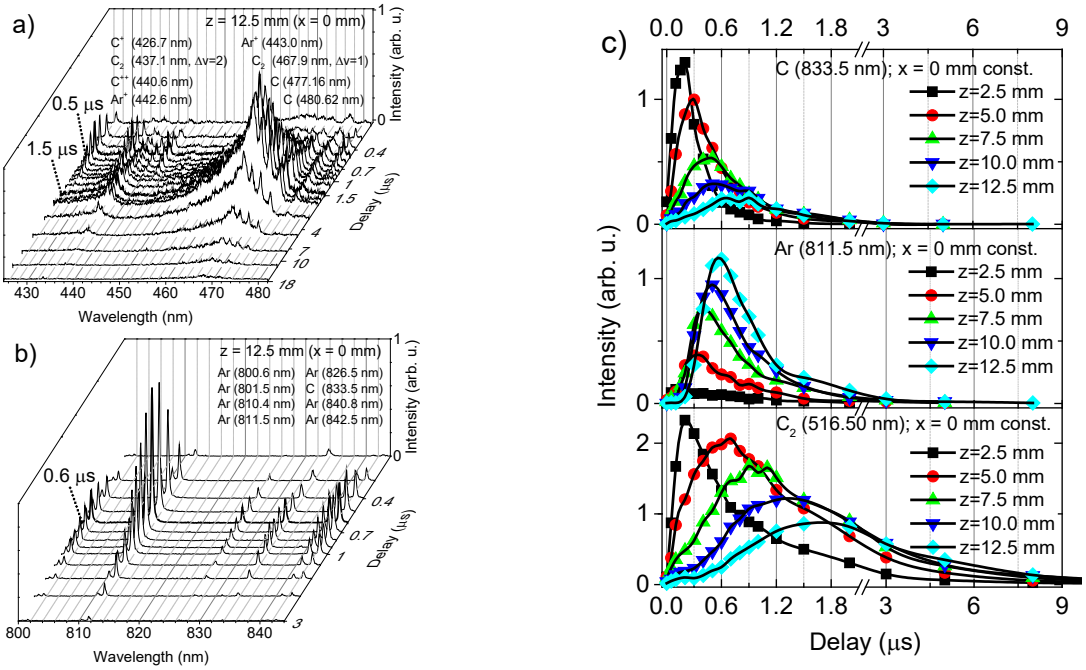


**Fig. 4.** a,b) Time-resolved emission spectra for two selected spectral regions, recorded at 12.5 mm from the target along the plasma z-axis, and c) the derived time-evolutions of representative atomic and molecular species at various distances from the target.

The space-distributions of emitting species and their correspondence with the plasma structures revealed by ICCD fast imaging (Fig. 1) can be obtained when the results from Fig. 4c are replotted as a function of $z$ for various time delays (see Fig. 5). The wider spreading of $C_2$ molecules in comparison with

atomic C becomes clearer, their emission maxima being located relatively close to the target, behind the fast plasma structure (see the corresponding ICCD images from Fig.1). Moreover, the maximum emission position of neutral Ar is shifting with time away from the target (Fig. 5b) and the maxima located at 7.5 mm and 10 mm (for 0.3 μs and 0.4 μs delays, respectively) perfectly match the fast plasma structure evolution evidenced by ICCD imaging in Fig.1.

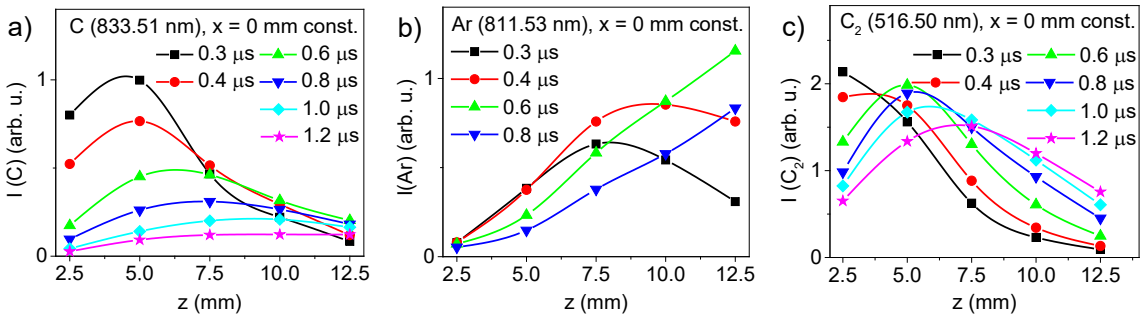


**Fig. 5.** Axial intensity distributions of the main radiating plasma species: a) atomic carbon, b) argon and c) carbon dimers, at various delays from the laser pulse.

In order to retrieve the composition of lateral plasma structures, OES measurements in radial direction were performed. Thus, for the distance of $z$=12.5 mm away from the target, we recorded the emission spectra at various delays after the laser pulse along the lateral direction, $x$. In Figs. 6a,b the time-evolution of spectra recorded for $x$=5 mm and $x$=12.5 mm (which in Fig. 1 correspond to the regions of intensified emission of radiation for the lateral arms, between 1μs and 3 μs), shows again a specific maximum of emissivity of each plasma species, at different moments of time. Thus, atomic C and Ar emit mostly between 0.3 μs and 1.8 μs, with a decreasing intensity when departing from the central axis (Fig. 6c). In a different manner, $C_2$ dimer emits mainly between 0.6 μs and 6 μs, more intense at $x$=5 mm, and less on the central axis and outer ($x$>5 mm) regions. As already done above for the axial dependence, the radial evolution from Fig. 6c is replotted as a function of $x$ for various delays in Fig. 7.

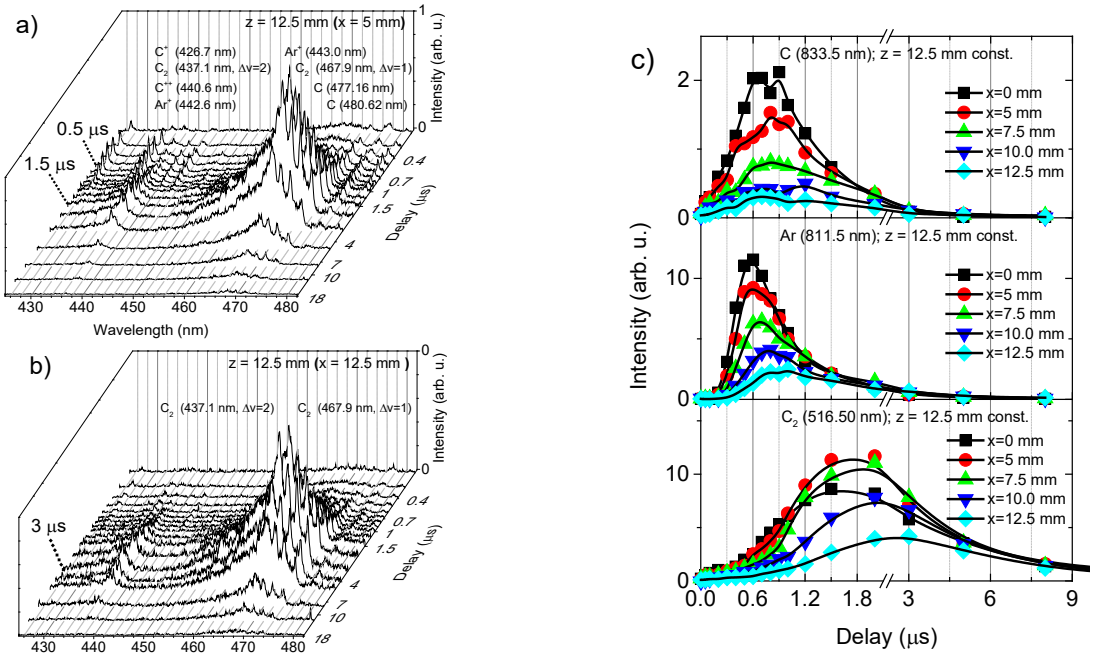


**Fig. 6.** a),b) Time-resolved emission spectra recorded at $z$=12.5 mm for the radial positions a) $x$=5 mm and b) $x$=12.5 mm, and c) derived time-evolutions of representative species.

Spectral lines intensity dependence with $x$-coordinate at $z$=12.5 mm agrees with previous sequential ICCD images: within the time frame 0.6-3 μs a maximum of $C_2$ emission is recorded for $x$=5 – 7.5 mm (see Fig. 7a), *i.e.* for the lateral arm seeds of V-shape plasma. This dependence is also valid for neutral C (Fig. 7b), but only at later times, 2 μs and 3 μs; most of its emission occurs in the axial region, at early times. We also note a decrease of the C emission after 0.8 μs, simultaneously with an increase of the $C_2$ emission, which let us infer an enhancement of the dimer to atom ratio in the lateral regions.

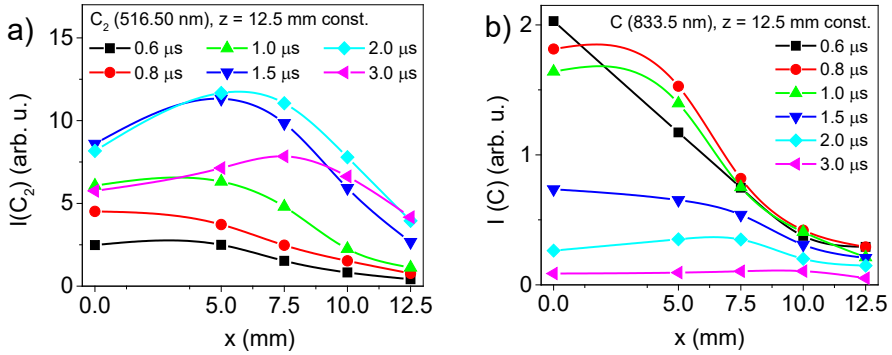


**Fig. 7.** Emission intensity radial evolutions of: a) molecular and b) atomic carbon selected spectral lines at various delays from the laser pulse.

The radial intensity variation of different plasma species evidenced here is less marked than the one recorded for the expansion in vacuum [24]. Starting from the plasma symmetry axis, it begins with a slight variation region (Fig. 7a,b), until a rapid decrease occurs, as one goes further in radial direction. For a better comparison of the two cases, it should be noted that for the plasma produced in vacuum the radial variations of the intensity of different species were determined close to the target surface and at early times (300 ns). The main difference between the variations of different emitting species with lateral $x$-distance, in vacuum and argon ambient gas, arises from the confinement of the plasma (which is more pronounced at higher delays and distances from the target) in the latter case. Also, the (fast) intensity decrease which should happen as we get closer to the symmetry axis (see Fig. 6b of [24]) is compensated in ambient gas by increased recombination processes of the ions (which in vacuum display a clear maximum on the axis, see Fig. 11 of [24]). The recombination processes in the axial region lead to an enhancement of both dimer and neutral carbon atoms and, consequently, to a slower radial variation of the emitting species. Therefore, we conclude that the effect of the ambient gas is to enhance the dimer formation for the lateral regions.

### *3.3. Temperature evaluations*

Among various methods to obtain the plasma temperature, probably the most used one considers relative intensities of ionic or atomic spectral lines in Boltzmann plots [39]. This depends critically on whether the plasma is in local thermodynamic equilibrium (LTE) or not, a good spectral resolution, optically thin plasma, and a low level of continuum (*i.e.* broadband) with respect to the line intensities [40]. All these conditions are clearly not met simultaneously for the entire space-time domain considered here; moreover, the energy spacing between the upper levels of the spectral lines considered for each species is relatively low. In these circumstances, an insight on the plasma energetics is provided below by estimating the vibrational temperature of $C_2$ emission and the temperature associated with the continuum spectrum.

#### *3.3.1 Temperature evaluation from vibrational spectra*

To characterize carbon laser-produced plasma, the vibrational temperature ($T_{vib}$) is often used, and it is deduced in the assumption of a Boltzmann distribution for the population of various excited (vibrational) levels of the $C_2$ molecule. The emission intensity of a vibrational transition ($I_{v'v''}$) is given by [41,42]:

$$ln\sum_{v"}(\lambda^4 I_{v'v"}) = C_1 - \frac{E(v')}{k_B T_{vib}} \quad (1)$$

where $v'$ and $v"$ are the vibrational quantum numbers of the upper and lower states, respectively, $\lambda$ is the $(v' \rightarrow v")$ transition wavelength, $E(v')$ is the energy of the upper vibrational level, $C_1$ is a constant, and $k_B$ are the Boltzmann constant. Thus, log-linear plot of $ln\sum_{v"}(\lambda^4 I_{v'v"})$ *vs.* $E(v')$ allow to obtain the vibrational temperature through the slope of the linear dependence. Our estimations were made using $\Delta v = -1,0,1,2$ vibrational sequences and the constants from [21]. We note that Eq. (1) does not take into account the rotational levels. Our spectral resolution does not allow resolving the rotational structure. Moreover, the vibrational temperatures were calculated by measuring the bandhead intensities, which usually encompass only a few rotational levels. A complete theoretical treatment would derive the temperature from a fit against theoretical spectra, where the rotational levels should be included [43-46], but this is beyond the scope of our work, as we do not have the required spectral resolution.

The calculated temperatures share the same order of magnitude with literature data [41,42] derived by using the same methodology. They are plotted in Fig. 8, as time-dependencies at various distances from the target – Fig. 8a in comparison with $C_2$ emission (516.50 nm vibrational band) intensity, and then as space-dependencies in axial and lateral directions at various time-delays – Figs. 8b,c.

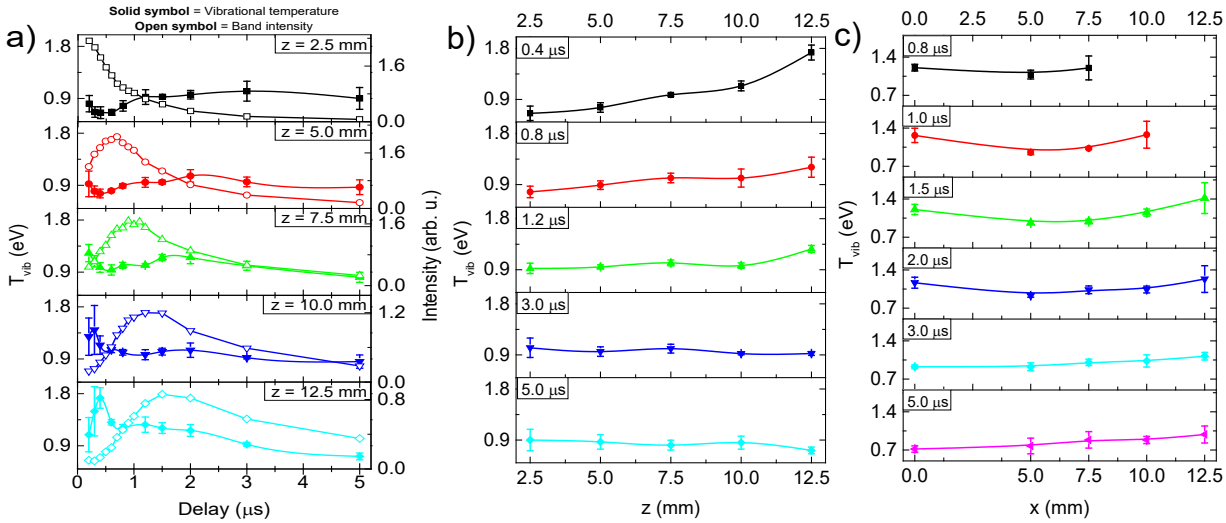


**Fig. 8.** Calculated vibrational temperature: a) time variation at different distances along the normal to the target, in comparison with $C_2$ emission (516.50 nm vibrational band) intensity, b) axial and c) radial evolutions (determined for z = 12.5 mm from the target) at various delays from the laser pulse. The error bars are obtained from the standard errors of the parameters deduced through the numerical fitting.

We generally observe fluctuations around $T_{vib}$ =0.9 eV and large error bars at short delays, probably due to a high level of continuum emission. Fig. 8a) reveals an initial temperature drop for *z*=(2.5; 5; 7.5) mm or an early maximum (better observable for *z*=12.5 mm), followed by a plateau region. This is related to the fast-emitted structure, which gives the arc-shape radiating structure (see Fig. 1) at (0.4-0.6) μs, corresponding to *z*=(10-12.5) mm from the target. Plasma re-heating far from the target is obviously the effect of ambient gas, having in view that the collisions it induces convert kinetic energy into thermal one. We note that high temperatures do not favor the $C_2$ formation and this is confirmed by superposing the $C_2$ emission (516.50 nm vibrational band) intensity on the temperature evolution (Fig. 8a). Finally, the plateau region is given by subsequent thermal ejection of particles from the target at later times. By converting these experimental data into axial evolutions (Fig. 8b), one can clearly notice the increasing trend of the temperature towards the region where the fast structure is located, and then an almost constant value for later times, as the plasma cools down.

Regarding the radial evolution of the vibrational temperature (Fig.8c), a shallow minimum can be noticed in the 0.8-2 μs time interval. This corresponds to the maximum emission regions of the lateral

radiating balls when looking back to the ICCD images in Fig. 1. As we move towards later times (3 to 5 μs), the axial plasma slowly cools down, simultaneously with energy being carried out of this region by the lateral plasma balls. In this scenario, the minimum temperature encountered for the region of the lateral plasma structures is somehow surprising. We can nevertheless speculate on a possible loss of (vibrational) excitation energy by the dimer formation process itself.

*3.3.2. Temperature evaluation from continuum emission*

The analysis of the continuum optical emission can provide useful insights on the plasma energetics, especially in the framework of nanoparticle formation [47]. Fig. 9a) shows typical power spectra presented in the form of log-linear plots of ln $(I\lambda^5)$ vs. $\lambda^{-1}$ for the spectral region (452.5 - 466.5) nm. The results are well fitted by a straight line, that in the assumption of a Boltzmann distribution is having the slope $hc/k_B T_{cont}$, with $h$ the Planck constant and $c$ is the speed of light. This allows computing the value of the temperature associated with the continuum spectrum [48].

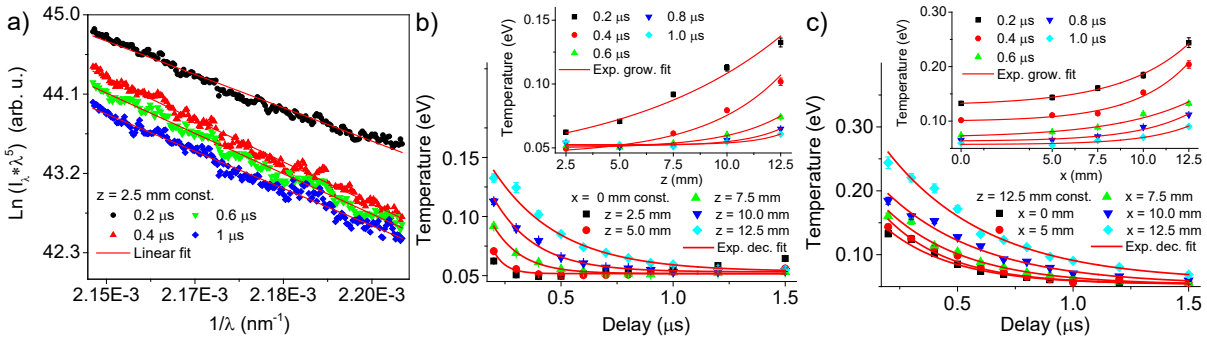


**Fig. 9.** a) Log-linear plots of ln $(I\lambda^5)$ vs. $\lambda^{-1}$ for the spectral range (452.5, 466.5) nm and temperature space-time evolution b) along the z-axis, and c) in *x*-lateral direction. The error bars are obtained from the standard errors of the parameters deduced through the numerical fitting.

The common feature is the time-decrease of the temperature for all analyzed regions, from a few thousand K to about 600 K. This can be well characterized by exponential decays with characteristic times that linearly increase with *z* (for *x*=0 mm), from about 50 ns (for *z*=5 mm) to 300 ns (for *z*=12.5 mm), and with *x* (for *z*=12.5 mm) from 300 ns (for *x*=0 mm) to 420 ns (for *x*=12.5 mm). Space evolution (insets in Fig. 9b,c) shows an increase of the continuum temperature with the distance from the target and in lateral direction for all time-sequences, almost similarly as the vibrational temperature (Fig. 8b). This can be given by kinetic to thermal energy conversion and/or non-radiative recombination processes, both promoted by collisions with the ambient gas.

*3.4. Electron density evaluations from atomic lines broadening and shifting*

To measure the electron density of the plasma, the Stark broadening mechanism of spectral lines is usually assumed [49,50,51]. The line full width at half maximum (FWHM) can be computed in the electron impact approximation and corrected for the relatively unimportant quasi-static ion broadening [39]. Together with the broadening, there is also a shift of the line center. An estimation of the FWHM, $\Delta\lambda_{1/2}$, and the line shift, $\Delta\lambda_{shift}$, for neutral atoms is given by [39]:

$$\Delta\lambda_{1/2} = 2W \cdot N_e + 3.5A \cdot {N_e}^{1/4}\left[1 - \frac{3}{4}N_D^{-1/3}\right] W \cdot N_e \quad (2)$$

$$\Delta\lambda_{shift} = D \cdot N_e \pm 2A \cdot {N_e}^{1/4}\left[1 - \frac{3}{4}N_D^{-1/3}\right] W \cdot N_e \quad (3)$$

where in both equations the first term is given by the electronic contribution, and the second one is the correction for the ions. $N_D$ is the number of particles in the Debye sphere, the coefficients $W$, $A$ and $D$ are independent of $N_e$ and slowly varying with the electron temperature $T_e$. The minus sign in Eq. (3) applies

to the high-temperature range for lines that have a negative value of *D/W* at low temperatures. For singly-charged ions, the relationships are obtained from Eqs. (2) and (3) by replacing the numerical coefficient 3/4 by 6/5 [39]. A list of *W*, *A*, *D* theoretical values is given in [39], while experimental values can be found in [52]. In the case of neutral atoms and singly-charged ions, it is usually assumed that the electron contribution dominates the Stark-broadened profile. Therefore, Eqs. (2) and (3) are reduced to the first term and a proportionality exists between the FWHM and the line shift, in the hypothesis that *D/W* is not temperature-dependent.

In our case we focused on the $\lambda$=833.5 nm line of neutral C, which is dominant in the 820-860 nm spectral range. Its profile is not significantly influenced by continuum radiation and fits well a Lorentzian function, allowing us to accurately derive the center and the FWHM of the line. In Fig. 10a we plot the time-evolution of these parameters for various *z* distances from the target surface.

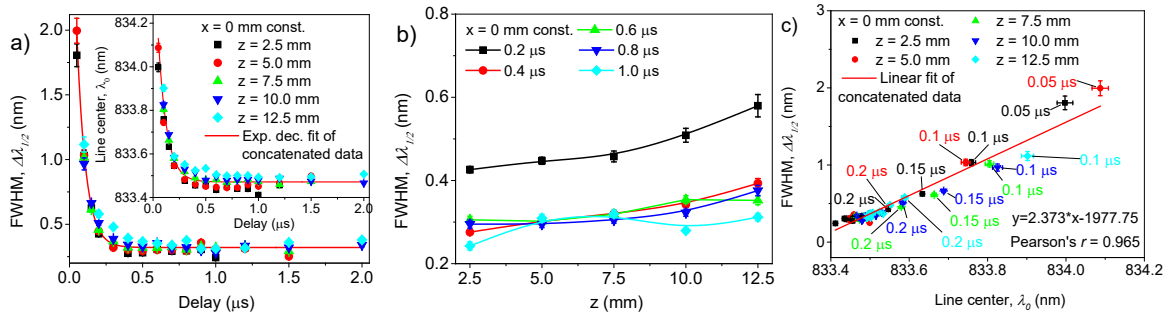


**Fig. 10.** a) Time-evolution of the center and FWHM of the neutral C 833.5 nm line at various *z*-distances from the target, b) on-axis space-evolution of the FWHM, and c) FWHM *vs.* center of line at various delays and axial positions. The error bars are obtained from the standard errors of the parameters deduced through the numerical fitting.

We observe that the FWHM decreases from $\Delta\lambda$ = 2.4 nm to $\Delta\lambda_{inst}$ = 0.25 nm, *i.e.* a value given by the instrumental broadening, with an exponential time decay constant of about $\tau$=60 ns in average. A similar behavior was observed for the center of the line, which is shifted by up to 1.5 nm at early times and tends to the theoretical value within 0.4 μs. These shifts have similar order of magnitude with values reported in [53]. We note that in the plots the values having an adjusted coefficient of determination lower that 0.95 were removed.

Line deconvolution with the instrumental Gaussian profile can be generally used to get the "pure" Stark width. However, having in view that our recorded spectra are of relatively low spectral resolution, we can simply subtract the instrumental width from the total one, to obtain rough estimations for the space-time evolution of the electron density. According with [54], for $N_e$=$10^{16}$ cm$^{-3}$, it was theoretically estimated $\Delta\lambda_{1/2} = 0.148$ Å and $\lambda_{shift} = 0.147$ Å at *T*=20000 K, while for *T*=10000 K, it resulted $\Delta\lambda_{1/2} = 0.127$ Å, and $\lambda_{shift} = 0.144$ Å. These values are by two orders of magnitude lower than our results and they have a weak dependence on the temperature, allowing us to estimate in this case electron densities of the order of $N_e$=$10^{18}$ cm$^{-3}$ (having the same order of magnitude as often reported in literature - for example see [53]), with the previous exponential time decay constant of $\tau$=60 ns.

Converting the results into space-dependencies of FWHM (proportional with electron density) at various time sequences (Fig. 10b), it results an increasing trend with *z*, behavior that agrees with the ones of the vibrational (Fig. 8b) and continuum temperatures (inset of Fig. 9b). When plotting the FWHM *vs.* the line center (Fig. 10c) for various time delays, we generally observe linear dependences for all distances from the target, with Pearson correlation coefficient $r > 0.95$. Since the slopes were similar, concatenated data were used to obtain a space-time average slope of 2.373 (*i.e.* a *W/D* ratio of 1.186) with Pearson *r*=0.96. Having in view Eqs. (2) and (3), these results confirm the negligible ion contribution, the weak temperature dependence of the *W/D* ratio, and its reasonable approximation with unitary value. The same behavior is observed when investigating the radial evolution (Fig. 11, for a distance from the target *z*=12.5 mm). In

Fig. 11a the spectral line FWHM and center show again exponential time-decays, with an average time constant $\tau$=90 ns. Converting data in space-dependences at various time sequences, the electron density shows a local maximum for $x$ = 7.5 - 10 mm, *i.e.* in the lateral arms observed in ICCD images (Fig. 1) and this maximum coincides with a vibrational temperature minimum (see above). These observations are to be interpreted in the overall formation/excitation/ionization balance of dimers and C/Ar neutrals and ions. Moreover, the FWHM *vs*. line center plot (Fig. 11c) leads to a *W*/*D* ratio of 0.892, again close to the assumed theoretical value of 1. All these are consistent proofs for the electron-impact approximation and for the axial-radial evolution scenario built for the transient plasma structures.

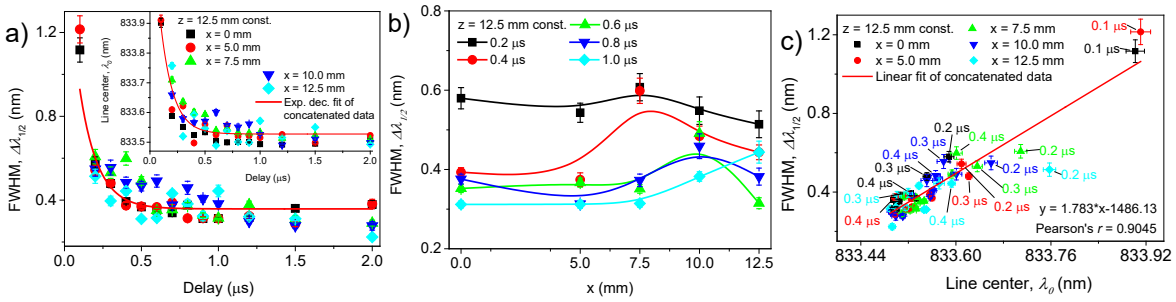


**Fig. 11.** a) Time-evolutions of the center and the FWHM of neutral C 833.5 nm line at various lateral $x$-distances, and b) linewidth evolution in lateral $x$-direction, and c) FWHM *vs.* center of line at various delays and lateral positions. The error bars are obtained from the standard errors of the parameters deduced through the numerical fitting.

## 4. Conclusions

An excimer laser-produced carbon plasma of unusual V-like shape expanding in Ar background gas was studied using fast-gate ICCD imaging and optical emission spectroscopy, to investigate the space-time distribution of molecular and atomic species. Among them, the $C_2$ dimer (which plays an important role in the formation of large molecules) was found in a previous study (expansion in vacuum [24]) to be enhanced mainly through three-body recombination. The plasma images recorded at various delays reveal the V-shape plasma structure that can be observed after the initial stages of expansion, similarly as in vacuum [24]. Along the normal direction to the target surface, there are initially fast ejected particles which are decelerated by collisions with the background gas, leaving behind them two radiating lateral arms. At later times ( $\gtrsim$ 2 μs), these arms transform into two plasma balls, flying almost parallel with the target normal, until they finally merge in a single structure. The corresponding velocities at initial stages were $v_{fast}(v_{fast}^x, v_{fast}^z) = (0, 1.5)\cdot 10^4$m/s, and $v_{slow}(v_{slow}^x, v_{slow}^z) = (2.1, 6.2)\cdot 10^3$m/s. After the initial stages, both structures are slowed down, and the time-dependence of the maximum emissivity positions obeys the well-known drag model.

The atomic and molecular species were monitored by using time-resolved OES of ≈1 mm$^2$ emitting regions of plasma. We observed that the atomic C is mostly present near the target, at early times, while the dimer persists for longer times and distances. The Ar emission was evidenced mostly far from the target. Spectral lines intensity radial evolution agrees with the sequential ICCD images: a maximum of $C_2$ emission is recorded for the lateral arms of the V-shape plasma, while a minimum is observed on the axis. This is also valid for neutral C, but only at later times, 2 μs and 3 μs; most of its emission occurs in the axial region at early times. Comparing these results with the previous ones for expansion in vacuum [24], we conclude that the effect of ambient gas is to increase the ratio between the dimer and the atomic C for the lateral regions.

The spectroscopic study also allowed calculation of vibrational and continuum temperatures, which evidences the role of the background Ar gas in re-heating the plasma far from the target. Finally, we used Stark-broadening and shifting of the 833.5 nm C line for electron density evaluations. By plotting the spectral line FWHM *vs*. central wavelength for various time delays and axial-radial positions, a

confirmation of the negligible ion contribution to the broadening/shifting mechanism was provided. Furthermore, the consistency of the temperature and density evolutions give solid proofs for the validity of the plasma dynamics scenario built for this unusual plume shape.

**Acknowledgements**
Part of this work was supported by the Romanian Space Agency (ROSA) within Space Technology and Advanced Research (STAR) Program (Project no.: 169/20.07.2017).

## References


[1] C. Phipps, Laser Ablation and its Applications, Springer, New York, 2007.

[2] T.E. Itina (Ed.), Laser Ablation - From Fundamentals to Applications, InTech, 2017. doi:10.5772/67961.

[3] P. Nica, S. Gurlui, M. Osiac, M. Agop, M. Ziskind, C. Focsa, Investigation of femtosecond laser-produced plasma from various metallic targets using the Langmuir probe characteristic, Phys. Plasmas. 24 (2017) 103119. doi:10.1063/1.5006076.

[4] S. Musazzi, U. Perini (Eds.), Laser-Induced Breakdown Spectroscopy, Springer, Berlin, Heidelberg, 2014. doi:10.1007/978-3-642-45085-3.

[5] R.E. Russo, X. Mao, J.J. Gonzalez, V. Zorba, J. Yoo, Laser ablation in analytical chemistry, Anal. Chem. 85 (2013) 6162–6177. doi:10.1021/ac4005327.

[6] R. Eason (Ed.), Pulsed Laser Deposition of Thin Films: Applications-led Growth of Functional Materials, Wiley-Interscience, New Jersey, 2007.

[7] D.H. Lowndes, D.B. Geohegan, A.A. Puretzky, D.P. Norton, C.M. Rouleau, Synthesis of novel thin-film materials by pulsed laser deposition, Science 273 (1996) 898–903. doi:10.1126/science.273.5277.898.

[8] T. Coman, D. Timpu, V. Nica, C. Vitelaru, A.P. Rambu, G. Stoian, M. Olaru, C. Ursu, Sequential PLD in oxygen/argon gas mixture of Al-doped ZnO thin films with improved electrical and optical properties, Appl. Surf. Sci. 418 (2017) 456–462. doi:10.1016/j.apsusc.2017.01.102.

[9] G. Dascalu, G. Pompilian, B. Chazallon, V. Nica, O. Caltun, S. Gurlui, C. Focsa, Rare earth doped cobalt ferrite thin films deposited by PLD, Appl. Phys. A 110 (2013) 915-922. doi: 10.1007/s00339-012-7196-8

[10] A.A. Puretzky, D.B. Geohegan, X. Fan, S.J. Pennycook, Dynamics of single-wall carbon nanotube synthesis by laser vaporization, Appl. Phys. A Mater. Sci. Process. 70 (2000) 153–160. doi:10.1007/s003390050027.

[11] A.A. Puretzky, H. Schittenhelm, X. Fan, M.J. Lance, L.F. Allard, D.B. Geohegan, Investigations of single-wall carbon nanotube growth by time-restricted laser vaporization, Phys. Rev. B. 65 (2002) 245425. doi:10.1103/PhysRevB.65.245425.

[12] C. Moise, M. Enachescu, High-Quality Carbon Nanomaterials Synthesized by Excimer Laser Ablation, in: Appl. Laser Ablation - Thin Film Depos. Nanomater. Synth. Surf. Modif., InTech, 2016: p. 13. doi:10.5772/65309. [13] H.M. Ruiz, F. Guzmán, M. Favre, H. Bhuyan, H. Chuaqui, E.S. Wyndham, Time- and space-resolved spectroscopic characterization of a laser carbon plasma plume in an argon background, Plasma Sources Sci. Technol. 21 (2012) 034014. doi:10.1088/0963-0252/21/3/034014.

[14] F. Guzmán, M. Favre, H.M. Ruiz, S. Hevia, L.S. Caballero, E.S. Wyndham, H. Bhuyan, M. Flores, S. Mändl, Pulsed laser deposition of thin carbon films in a neutral gas background, J. Phys. D. Appl. Phys. 46 (2013) 215202. doi:10.1088/0022-3727/46/21/215202.

[15] C. Focsa, P. Nemec, M. Ziskind, C. Ursu, S. Gurlui, V. Nazabal, Laser ablation of $As_xSe_{100-x}$ chalcogenide glasses: Plume investigations, Appl. Surf. Sci. 255 (2009) 5307–5311. doi:10.1016/j.apsusc.2008.07.204.

[16] O.G. Pompilian, S. Gurlui, P. Nemec, V. Nazabal, M. Ziskind, C. Focsa, Plasma diagnostics in pulsed laser deposition of GaLaS chalcogenides, Appl. Surf. Sci. 278 (2013) 352–356. doi:10.1016/j.apsusc.2012.11.069.

[17] C. Ursu, O.G. Pompilian, S. Gurlui, P. Nica, M. Agop, M. Dudeck, C. Focsa, $Al_2O_3$ ceramics under high-fluence irradiation: plasma plume dynamics through space- and time-resolved optical emission spectroscopy, Appl. Phys. A. 101 (2010) 153–159. doi:10.1007/s00339-010-5775-0.

[18] C. Ursu, S. Gurlui, C. Focsa, G. Popa, Space- and time-resolved optical diagnosis for the study of laser ablation plasma dynamics, Nucl. Instrum. Meth. B 267 (2009) 446–450. doi:10.1016/j.nimb.2008.10.057.
[19] A. Van Orden, R.J. Saykally, Small carbon clusters: Spectroscopy, structure, and energetics, Chem. Rev. 98 (1998) 2313–2358. doi:10.1021/cr970086n.
[20] D.E. Motaung, M.K. Moodley, E. Manikandan, N.J. Coville, In situ optical emission study on the role of $C_2$ in the synthesis of single-walled carbon nanotubes, J. Appl. Phys. 107 (2010) 044308. doi:10.1063/1.3311563.
[21] A. Tanabashi, T. Hirao, T. Amano, P.F. Bernath, The Swan system of $C_2$ : A global analysis of Fourier transform emission spectra, Astrophys. J. Suppl. Ser. 169 (2007) 472–484. doi:10.1086/510742.
[22] C. Ursu, P.E. Nica, Diagnosis of carbon laser produced plasma by using an electrostatic energy analyzer, J. Optoelectron. Adv. Mater. 15 (2013) 42–45.
[23] P.E. Nica, G.B. Rusu, O.G. Dragos, C. Ursu, Effect of excimer laser beam spot size on carbon laser-produced plasma dynamics, IEEE Trans. Plasma Sci. 42 (2014) 2694–2695. doi:10.1109/TPS.2014.2350532.
[24] C. Ursu, P. Nica, C. Focsa, Excimer laser ablation of graphite: The enhancement of carbon dimer formation, Appl. Surf. Sci. 456 (2018) 717–725. doi:10.1016/j.apsusc.2018.06.217.
[25] C. Ursu, P. Nica, C. Focsa, M. Agop, Fractal method for modeling the peculiar dynamics of transient carbon plasma generated by excimer laser ablation in vacuum, Complexity. 2018 (2018) 1814082. doi:10.1155/2018/1814082.
[26] M. Agop, P.E. Nica, S. Gurlui, C. Focsa, V.P. Paun, M. Colotin, Implications of an extended fractal hydrodynamic model, Eur. Phys. J. D. 56 (2010) 405–419. doi:10.1140/epjd/e2009-00304-5.
[27] S.A. Irimiciuc, B.C. Hodoroaba, G. Bulai, S. Gurlui, D. Craciun, V. Craciun, Multiple structure formation and molecule dynamics in transient plasmas generated by laser ablation on graphite, EMRS2019 European Materials Research Society Spring Meeting, poster V.P3.11, Nice, France, 27-31 May 2019
[28] S.S. Harilal, B. O'Shay, M.S. Tillack, C.V. Bindhu, F. Najmabadi, Fast photography of a laser generated plasma expanding across a transverse magnetic field, IEEE Trans. Plasma Sci. 33 (2005) 474–475. doi:10.1109/TPS.2005.844965.
[29] K.F. Al-Shboul, S.S. Harilal, A. Hassanein, Gas dynamic effects on formation of carbon dimers in laser-produced plasmas, Appl. Phys. Lett. 99 (2011) 131506. doi:10.1063/1.3645631.
[30] A. De Giacomo, M. Dell'Aglio, R. Gaudiuso, O. De Pascale, Effects of the background environment on formation, evolution and emission spectra of laser-induced plasmas, Spectrochim. Acta B 78 (2012) 1–19. doi: 10.1016/j.sab.2012.10.003.
[31] S. Amoruso, J. Schou, J.G. Lunney, Influence of the atomic mass of the background gas on laser ablation plume propagation, Appl. Phys. A Mater. Sci. Process. 92 (2008) 907–911. doi:10.1007/s00339-008-4591-2.
[32] R.F. Wood, J.N. Leboeuf, D.B. Geohegan, A.A. Puretzky, K.R. Chen, Dynamics of plume propagation and splitting during pulsed-laser ablation, Phys. Rev. Lett. 79 (1997) 1571–1574. doi:10.1103/PhysRevLett.79.1571.
[33] C. Focsa, S. Gurlui, P. Nica, M. Agop, M. Ziskind, Plume splitting and oscillatory behavior in transient plasmas generated by high-fluence laser ablation in vacuum, Appl. Surf. Sci. 424 (2017) 299–309. doi:10.1016/j.apsusc.2017.03.273.
[34] K.K. Anoop, S.S. Harilal, R. Philip, R. Bruzzese, S. Amoruso, Laser fluence dependence on emission dynamics of ultrafast laser induced copper plasma, J. Appl. Phys. 120 (2016) 185901. doi:10.1063/1.4967313.

[35] D.B. Geohegan, Fast intensified-CCD photography of $YBa_2Cu_3O_{7-x}$ laser ablation in vacuum and ambient oxygen, Appl. Phys. Lett. 60 (1992) 2732–2734. doi:10.1063/1.106859.
[36] S.S. Harilal, C. V. Bindhu, M.S. Tillack, F. Najmabadi, A.C. Gaeris, Internal structure and expansion dynamics of laser ablation plumes into ambient gases, J. Appl. Phys. 93 (2003) 2380–2388. doi:10.1063/1.1544070.
[37] C.G. Parigger, Measurements of Gaseous Hydrogen–Nitrogen Laser-Plasma, Atoms. 7 (2019) 61. doi:10.3390/atoms7030061.
[38] Y. Ralchenko, A.E. Kramida, J. Reader, and NIST ASD Team (2008). NIST Atomic Spectra Database (version 3.1.5) (Online: http://physics.nist.gov/asd3). National Institute of Standards and Technology, Gaithersburg, MD.
[39] H.R. Griem, Principles of Plasma Spectroscopy, Cambridge University Press, Cambridge, 2005.
[40] G. Cristoforetti, A. De Giacomo, M. Dell'Aglio, S. Legnaioli, E. Tognoni, V. Palleschi, N. Omenetto, Local thermodynamic equilibrium in laser-induced breakdown spectroscopy: Beyond the McWhirter criterion, Spectrochim. Acta B. 65 (2010) 86–95. doi:10.1016/j.sab.2009.11.005.
[41] K.F. Al-Shboul, S.S. Harilal, A. Hassanein, Emission features of femtosecond laser ablated carbon plasma in ambient helium, J. Appl. Phys. 113 (2013) 163305. doi:10.1063/1.4803096.
[42] Y. Yamagata, A. Sharma, J. Narayan, R.M. Mayo, J.W. Newman, K. Ebihara, Comparative study of pulsed laser ablated plasma plumes from single crystal graphite and amorphous carbon targets. Part I. Optical emission spectroscopy, J. Appl. Phys. 88 (2000) 6861–6867. doi:10.1063/1.1321783.
[43] C.G. Parigger, A.C. Woods, D.M. Surmick, G. Gautam, M.J. Witte, J.O. Hornkohl, Computation of diatomic molecular spectra for selected transitions of aluminum monoxide, cyanide, diatomic carbon, and titanium monoxide, Spectrochim. Acta Part B At. Spectrosc. 107 (2015) 132–138. doi:10.1016/j.sab.2015.02.018.
[44] C.G. Parigger, Atomic and molecular emissions in laser-induced breakdown spectroscopy, Spectrochim. Acta Part B At. Spectrosc. 79–80 (2013) 4–16. doi:10.1016/j.sab.2012.11.012.
[45] C.G. Parigger, J.O. Hornkohl, A.M. Keszler, L. Nemes, Measurement and analysis of atomic and diatomic carbon spectra from laser ablation of graphite, Appl. Opt. 42 (2003) 6192. doi:10.1364/AO.42.006192.
[46] L. Nemes, S. Irle, Spectroscopy, Dynamics and Molecular Theory of Carbon Plasmas and Vapors, World Scientific, 2011. doi:10.1142/7138.
[47] S. Amoruso, R. Bruzzese, N. Spinelli, R. Velotta, M. Vitiello, X. Wang, G. Ausanio, V. Iannotti, L. Lanotte, Generation of silicon nanoparticles via femtosecond laser ablation in vacuum, Appl. Phys. Lett. 84 (2004) 4502–4504. doi:10.1063/1.1757014.
[48] H.-J. Kunze, Introduction to Plasma Spectroscopy, Springer Berlin Heidelberg, Berlin, Heidelberg, 2009. doi:10.1007/978-3-642-02233-3.
[49] S. Amoruso, R. Bruzzese, N. Spinelli, R. Velotta, Characterization of laser-ablation plasmas, J. Phys. B At. Mol. Opt. Phys. 32 (1999) R131–R172. doi:10.1088/0953-4075/32/14/201.
[50] J. Dardis, J.T. Costello, Stagnation layers at the collision front between two laser-induced plasmas: A study using time-resolved imaging and spectroscopy, Spectrochim. Acta Part B At. Spectrosc. 65 (2010) 627–635. doi:10.1016/j.sab.2010.03.005.
[51] R.P. Singh, S.L. Gupta, R.K. Thareja, Spectroscopic investigation of colliding plasma plumes, Spectrochim. Acta Part B At. Spectrosc. 88 (2013) 54–62. doi:10.1016/j.sab.2013.08.006.
[52] N. Konjević, A. Lesage, J.R. Fuhr, W.L. Wiese, Experimental Stark widths and shifts for spectral lines of neutral and ionized atoms, J. Phys. Chem. Ref. Data. 31 (2002) 819–927. doi:10.1063/1.1486456.

[53] S.S. Harilal, C. V. Bindhu, R.C. Issac, V.P.N. Nampoori, C.P.G. Vallabhan, Electron density and temperature measurements in a laser produced carbon plasma, J. Appl. Phys. 82 (1997) 2140–2146. doi:10.1063/1.366276.
[54] H.R. Griem, Spectral line broadening by plasmas, Academic Press, New York, 1974.

**Figure caption**

**Fig. 1.** Fast-gate (50 ns) ICCD images of V-shape carbon plasma expanding in argon gas (circles indicate the regions used for OES measurements).

**Fig. 2.** a) Space position of maximum emission intensity at various time delays for the fast central plasma (red spot) and the slow lateral structures (black spot) and b) resulting expansion velocities.

**Fig. 3.** Typical plasma emission spectra recorded at $z$=12.5 mm away from the target, on the plasma symmetry axis ($x$=0, black curves), and at $x$=12.5 mm in radial direction (red curves) corresponding to a) $C_2$ Swan system and b) atomic Ar spectral regions, respectively.

**Fig. 4.** a,b) Time-resolved emission spectra for two selected spectral regions, recorded at 12.5 mm from the target along the plasma z-axis, and c) the derived time-evolutions of representative atomic and molecular species at various distances from the target.

**Fig. 5.** Axial intensity distributions of the main radiating plasma species: a) atomic carbon, b) argon and c) carbon dimers, at various delays from the laser pulse.

**Fig. 6.** a),b) Time-resolved emission spectra recorded at $z$=12.5 mm for the radial positions a) $x$=5 mm and b) $x$=12.5 mm, and c) derived time-evolutions of representative species.

**Fig. 7.** Emission intensity radial evolutions of: a) molecular and b) atomic carbon selected spectral lines at various delays from the laser pulse.

**Fig. 8.** Calculated vibrational temperature: a) time variation at different distances along the normal to the target, b) axial and c) radial evolutions (determined for z = 12.5 mm from the target) at various delays from the laser pulse. The error bars are obtained from the standard errors of the parameters deduced through the numerical fitting.

**Fig. 9.** a) Log-linear plots of $\ln(I\lambda^5)$ vs. $\lambda^{-1}$ for the spectral range (452.5, 466.5) nm and temperature space-time evolution b) along the z-axis, and c) in $x$-lateral direction. The error bars are obtained from the standard errors of the parameters deduced through the numerical fitting.

**Fig. 10.** a) Time-evolution of the center and FWHM of the neutral C 833.5 nm line at various $z$-distances from the target, b) on-axis space-evolution of the FWHM, and c) FWHM *vs.* center of line at various delays and axial positions. The error bars are obtained from the standard errors of the parameters deduced through the numerical fitting.

**Fig. 11.** a) Time-evolutions of the center and the FWHM of neutral C 833.5 nm line at various lateral $x$-distances, and b) linewidth evolution in lateral $x$-direction, and c) FWHM *vs.* center of line at various delays and lateral positions. The error bars are obtained from the standard errors of the parameters deduced through the numerical fitting.